

## MIT Open Access Articles

*X-ray imaging crystal spectroscopy  
for use in plasma transport research*

The MIT Faculty has made this article openly available. **Please share** how this access benefits you. Your story matters.

**Citation:** Reinke, M. L., Y. A. Podpaly, M. Bitter, I. H. Hutchinson, J. E. Rice, L. Delgado-Aparicio, C. Gao, et al. "X-ray imaging crystal spectroscopy for use in plasma transport research." *Review of Scientific Instruments* 83, no. 11 (2012): 113504. © 2012 American Institute of Physics

**As Published:** <http://dx.doi.org/10.1063/1.4758281>

**Publisher:** American Institute of Physics (AIP)

**Persistent URL:** <http://hdl.handle.net/1721.1/84059>

**Version:** Final published version: final published article, as it appeared in a journal, conference proceedings, or other formally published context

**Terms of Use:** Article is made available in accordance with the publisher's policy and may be subject to US copyright law. Please refer to the publisher's site for terms of use.



**X-ray imaging crystal spectroscopy for use in plasma transport research**

M. L. Reinke, Y. A. Podpaly, M. Bitter, I. H. Hutchinson, J. E. Rice, L. Delgado-Aparicio, C. Gao, M. Greenwald, K. Hill, N. T. Howard, A. Hubbard, J. W. Hughes, N. Pablant, A. E. White, and S. M. Wolfe

Citation: [Review of Scientific Instruments](#) **83**, 113504 (2012); doi: 10.1063/1.4758281

View online: <http://dx.doi.org/10.1063/1.4758281>

View Table of Contents: <http://scitation.aip.org/content/aip/journal/rsi/83/11?ver=pdfcov>

Published by the [AIP Publishing](#)

---

**Nor-Cal Products**



Manufacturers of High Vacuum  
Components Since 1962

[www.n-c.com](http://www.n-c.com)  
800-824-4166

- Chambers
- Motion Transfer
- Flanges & Fittings
- Viewports
- Foreline Traps
- Feedthroughs
- Valves



## X-ray imaging crystal spectroscopy for use in plasma transport research

M. L. Reinke,<sup>1</sup> Y. A. Podpaly,<sup>1</sup> M. Bitter,<sup>2</sup> I. H. Hutchinson,<sup>1</sup> J. E. Rice,<sup>1</sup>  
L. Delgado-Aparicio,<sup>2</sup> C. Gao,<sup>1</sup> M. Greenwald,<sup>1</sup> K. Hill,<sup>2</sup> N. T. Howard,<sup>1</sup> A. Hubbard,<sup>1</sup>  
J. W. Hughes,<sup>1</sup> N. Pablant,<sup>2</sup> A. E. White,<sup>1</sup> and S. M. Wolfe<sup>1</sup>

<sup>1</sup>MIT-Plasma Science and Fusion Center, Cambridge, Massachusetts 02139, USA

<sup>2</sup>Princeton Plasma Physics Laboratory, Princeton, New Jersey 08543, USA

(Received 31 May 2012; accepted 24 September 2012; published online 26 November 2012)

This research describes advancements in the spectral analysis and error propagation techniques associated with x-ray imaging crystal spectroscopy (XICS) that have enabled this diagnostic to be used to accurately constrain particle, momentum, and heat transport studies in a tokamak for the first time. Doppler tomography techniques have been extended to include propagation of statistical uncertainty due to photon noise, the effect of non-uniform instrumental broadening as well as flux surface variations in impurity density. These methods have been deployed as a suite of modeling and analysis tools, written in interactive data language (IDL) and designed for general use on tokamaks. Its application to the Alcator C-Mod XICS is discussed, along with novel spectral and spatial calibration techniques. Example ion temperature and radial electric field profiles from recent I-mode plasmas are shown, and the impact of poloidally asymmetric impurity density and natural line broadening is discussed in the context of the planned ITER x-ray crystal spectrometer. © 2012 American Institute of Physics. [<http://dx.doi.org/10.1063/1.4758281>]

### I. INTRODUCTION

Although measurements of the Doppler shift and broadening in x-ray line emission have long been used to gain insight into tokamak plasmas,<sup>1</sup> this technique has been limited by the signal being averaged over the plasma volume. Using a spherically bent crystal and high-resolution x-ray imaging detectors, this limitation has recently been overcome, and x-ray imaging crystal spectroscopy (XICS) has been demonstrated on a number of magnetic confinement fusion devices.<sup>2–5</sup> Employing the so-called Doppler tomography techniques,<sup>6,7</sup> line-integrated spectra are used to calculate the moments about the rest wavelength, which can be inverted to find local plasma flow and temperature. This research describes extensions to Doppler tomography as well as novel methods of calibration and alignment that have allowed XICS data to be used in particle, momentum, and heat transport studies of Alcator C-Mod plasmas.<sup>8–11</sup>

Section II briefly introduces the spectrometer hardware while Sec. III describes the Doppler tomography method, with new techniques described in more detail in the Appendix. Section IV introduces the set of analysis routines to analyze raw spectra, and discusses spectral and spatial calibration techniques used for the Alcator C-Mod spectrometer. Section V presents selected experimental results enabled by these analysis upgrades while Sec. VI discusses the future of XICS and concerns regarding its application in ITER and other high temperature plasmas.

### II. SPECTROMETER HARDWARE

In Alcator C-Mod XICS is accomplished using the high resolution x-ray spectrometer with spatial resolution (HIREXSR), building on experience with an earlier, multi-chord von Hamos system.<sup>12</sup> The details of the HIREXSR

hardware are discussed elsewhere,<sup>2,13</sup> although modifications to the optical alignment have been completed to correct for vignetting.

Two sets of crystals and detectors are kept inside a He-filled enclosure, separated from the tokamak vacuum by a 50  $\mu\text{m}$  Be window. A spherically bent, 50 mm diameter quartz crystal is used to Bragg reflect and focus radiation from  $\text{Ar}^{17+}$ , while a  $64 \times 27 \text{ mm}^2$  quartz crystal is used to analyze  $\text{Ar}^{16+}$  emission. The radius of curvature of the circular crystal is 1.385 m while the rectangular crystal is 1.443 m. The x-ray spectra are measured using Dectris PILATUS 100K detectors,<sup>14</sup> made up of  $487 \times 195$  pixels, each  $0.172 \times 0.172 \text{ mm}^2$ . Frame rates up to 200 Hz have been demonstrated, consisting of a 2 ms exposure and a 3 ms cycle time, while 50 Hz operation with a 17 ms exposure time is standard. An array of three PILATUS detectors is used to image  $3.94 < \lambda < 4.00 \text{ \AA}$  ( $\text{Ar}^{16+}$ ) over the entire poloidal cross section of Alcator C-Mod, while a single detector views  $3.72 < \lambda < 3.86 \text{ \AA}$  ( $\text{Ar}^{17+}$ ) for  $r/a < 0.6$ . Recently a 35 mm diameter,  $R_c = 1.442 \text{ m}$  quartz crystal has also been used in the core viewing system to measure time-evolving  $\text{Ca}^{18+}$  emission for impurity transport validation experiments.<sup>15</sup>

The  $(R, Z)$  locations of the crystals,  $(3687, 0)_{\text{He}}$  and  $(3782, 54)_{\text{H}}$  mm, relative to the center of the tokamak are determined with sufficient accuracy by referencing fiducials in the spectrometer to C-Mod's vacuum vessel. The port and vessel structure acts to vignette part of the He-like spectra which is the reason why the w/z intensity ratio (see Figure 2) is smaller than expected throughout this research. The z-line is unvignetted and is used for Doppler tomography. It provides the extended spatial coverage because it is populated by recombination and it is relatively simple to model the additional spectral features due to dielectronic satellite lines. Unexpectedly, the partial vignetting of the He-like spectrum is actually somewhat useful in that it gives an *in situ* means to

calculate the tangency radius of the spectrometer by comparing the expected and observed  $w/z$  line ratio. The inclination of the spectrometer with respect to the tokamak is also difficult to measure with sufficient accuracy since at  $\sim 3.5$  m from the core, an uncertainty of  $0.1^\circ$  corresponds to a 5 mm shift in the chords. Instead, the line-averaged ion temperature profile is assumed to be up/down symmetric and inclination defined accordingly.

### III. DOPPLER TOMOGRAPHY

Measured spectra are the result of viewing the emission integrated along a line of sight through a volumetric emitter. For x-ray line-emission, the fine-structure is resolved and the Zeeman effect is negligible, but natural line broadening can be important due to the strong increase in transition rates with impurity charge,  $A_{ij} \sim Z^4$ . For argon, ion temperatures on the order of a few hundred eV produce large Doppler broadening relative to the natural broadening. While this combination of Doppler and natural line broadening will result in a Voigt line profile being emitted by the plasma, a pure Gaussian line shape is assumed for the time being. The input spectral power,  $P_{in}^\lambda$  in [ph/s Å] or equivalent units, measured along a chord through the plasmas is then,

$$P_{in}^\lambda = \sum_i^p V_i \frac{\varepsilon_{o,i}}{w_i \sqrt{2\pi}} \exp \left[ -\frac{(\lambda - \lambda_o - \frac{\lambda_o}{c} (\hat{l} \cdot \mathbf{v}_i))^2}{2w_i^2} \right], \quad (1)$$

where the typical path integral has been replaced by a sum over discrete volume elements,  $V_i$ , or voxels, in the plasmas and  $\hat{l}$  is the unit vector of the line of sight. Here, total emissivity,  $\varepsilon_{o,i}$ , the velocity,  $\mathbf{v}_i$ , and the line width  $w_i^2 = \lambda_o^2 k_B T_{z,i} / m_z c^2$ , are indexed by the location in the plasma,  $i$ , and are the quantities of interest. In order to transform this nonlinear relationship between measurements and plasma properties, moments of both sides of (1) are taken about the rest wavelength,  $\lambda_o$ :

$$M_n = \int d\lambda P_{in}^\lambda (\lambda - \lambda_o)^n. \quad (2)$$

For the left-hand side, this is simply a manipulation of experimental spectra, while the right-hand side integrates over the Gaussian. If there are multiple views through the plasma, then the  $n^{\text{th}}$  moment for the  $j^{\text{th}}$  view through the plasma,  $M_{n,j}$ , is,

$$\begin{aligned} M_{0,j} &= \sum_i^p V_{ji} \varepsilon_{o,i}, \\ M_{1,j} &= \frac{\lambda_o}{c} \sum_i^p V_{ji} \varepsilon_{o,i} (\hat{l}_j \cdot \mathbf{v}_i), \\ M_{2,j} &= \sum_i^p V_{ji} \varepsilon_{o,i} \left( \frac{\lambda_o^2}{c^2} (\hat{l}_j \cdot \mathbf{v}_i)^2 + w_i^2 \right). \end{aligned} \quad (3)$$

These are the so-called moment equations, and have been discussed in the context of Doppler tomography in prior work.<sup>2,6,7</sup> The 0<sup>th</sup> moment is just the conventional tomography problem used to find the emissivity from the line-integrated power knowing the path lengths through the

plasma:

$$\vec{M}_0 = \mathbf{V} \cdot \vec{\varepsilon}. \quad (4)$$

A standard method of solving this type of inverse problem is to find the solution which minimizes the difference between modeled and measured data in a least-squares sense, subject to a regularization constraint:

$$\vec{\varepsilon} = (\mathbf{V}^T \cdot \mathbf{V} + \epsilon \mathbf{C}^T \mathbf{C})^{-1} \cdot \mathbf{V}^T \cdot \vec{M}_0. \quad (5)$$

When analyzing HIREXSR data,  $\mathbf{C}$  is the standard 2nd derivative matrix used in regularization, except on-axis where  $\mathbf{C}$  then becomes the 1st derivative matrix. This has the effect of smoothing the derived radial profile and works to force the radial derivative to vanish as  $r/a$  approaches 0. The default regularization parameter,  $\epsilon = 1.0$ , is multiplied by the maximum value of the  $\mathbf{V}$  matrix. The other two moment equations in (3) can also be solved sequentially in a similar manner for the velocity weighted emissivity,  $\varepsilon_v$ , and the temperature weighted emissivity profile,  $\varepsilon_T$ .

The Appendix details extensions that have been made to the Doppler tomography method to account for the propagation of photon statistical error and to handle non-uniform instrumental broadening, but there still remains other sources of uncertainty in applying the Doppler tomography technique. Systematic error in inversion setup such as the number of radial grid points or the level of regularization,  $\epsilon$ , are not included in this error. Thus one should treat the uncertainties derived in the Appendix as being a minimum error due to the collection of a limited number of photons propagating through the inversion. Investigations into the magnitude of channel-to-channel variations in the HIREXSR instrument function are ongoing. The ability to specify non-uniform instrumental broadening has been built into the analysis, but the impact of a spatially varying instrumental width on the derived temperature profiles is not included in the experimental results presented in the remainder of this research.

### IV. THE HIREXSR ANALYSIS CODE

The conventional Doppler tomography techniques as well as the extensions discussed in Sec. III have been deployed as the HIREXSR analysis code (THACO), developed in interactive data language (IDL) for use with the MD-SPlus data management system, both standard tools in plasma physics and fusion science. Effort has been made to avoid low-level hard-coding of Alcator C-Mod specifics in order to make the software transferable to other tokamaks. The code assumes a spherically bent Bragg reflector, making THACO usable for multilayer-mirror based instruments as well.<sup>16</sup> The spectrometer is completely described in a compact ASCII format that is used by both the inversion and forward modeling tools, enabling the software to be used for scoping and design studies for new spectrometers. THACO will be described in substantial detail in Ref. 17, while highlights of the analysis workflow are described here.

## A. Calibration

To determine the velocity to within  $\sim 1$  km/s from the Doppler shift, the absolute wavelength needs to be known to within 0.03% of the rest wavelength. The absence of intense, spatially extended, monochromatic sources in the soft x-ray wavelength range represents a limiting factor in the accuracy of XICS. In the visible wavelength range, pencil lamps are used to calibrate the instrument function and rest wavelengths. Techniques using K-shell and L-shell line emission from electron bombardment sources are being investigated, but cannot currently provide the necessary photon flux to fill the optics in a similar manner as the plasma.

Instead, an *in situ* calibration technique using locked mode plasmas seeded with argon was developed at Alcator C-Mod. Non-axisymmetric coils, normally used to zero out the error field<sup>18</sup> are driven to induce a locked mode. This transfers momentum to the error field coils, slowing the plasma towards being at rest in the lab frame. The argon species is assumed to have zero rotation across the entire plasma, supported on-axis by measurements from Ar<sup>17+</sup> using a calibrated von Hamos spectrometer, and off-axis by Ar<sup>16+</sup> charge exchange recombination spectroscopy (CXRS) measurements.<sup>19</sup> Locked mode rotation profile measurements using CXRS made in other tokamaks also support this hypothesis,<sup>20,21</sup> but the accuracy on the level required for XICS is questionable. In principle, any Ohmic plasma could be used in place of the locked-mode, increasing the uncertainty in the rotation profile. This approach could be acceptable for analyzing auxiliary-heated plasmas where rotation speeds are far in excess of the Ohmic baseline.

An example of an image from the core He-like Ar detector is shown in Figure 1(a) for a typical locked mode plasma. Argon fraction and integration time are increased well beyond typical levels used for transport analysis in order to get excellent statistics,  $10^4$  photons/pixel peak intensity, without averaging over spatial regions on the detector. For each of the 487 rows on the detector, the spectrum is fitted in pixel space

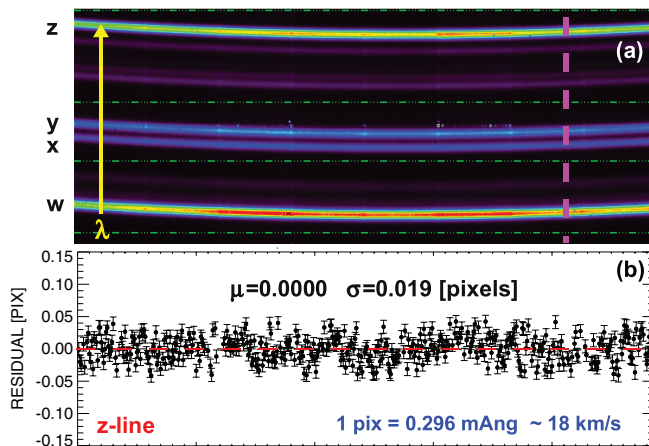


FIG. 1. Image from the central PILATUS detector in the He-like Ar viewing system for a locked mode plasma used for spatial and spectral calibration (a). The peak position of the line emission is fit to an ellipse which shows a very small residual (b).

to the sum of Gaussians to find the peak position of the w, x, y, and z lines, referenced using standard Gabriel notation. The curve of the spectral lines evident in Figure 1(a) can be shown analytically to be an ellipse which depends on the position and orientation of the detector plane relative to the center of the crystal.<sup>17</sup> Each of the four spectral line shapes is fitted to an ellipse, with the residual shown in Figure 1(b) for the z-line. The residual is zero to four significant figures and standard deviation of 0.02 pixels. With the pixel locations of the four ellipses known, the rest wavelengths of these lines are used to determine the wavelength mapping as function of pixel location, accounting for the slight nonlinear dispersion. For the He-like z-line, 1 pixel is found to be equivalent to  $\Delta\lambda = 0.296 \text{ m\AA}$ , corresponding to an  $\sim 22$  km/s Doppler shift at  $\lambda_0 = 3.994 \text{ \AA}$ . Statistically, the uncertainty in the elliptical fit corresponds to 0.44 km/s uncertainty in the observed Doppler shift. Because of the small tangency radii of the HIREXSR view, this shift corresponds to  $\sim 1.5$  km/s minimum uncertainty in the reported toroidal velocity. This calibration technique also accounts for the line-shift induced by finite crystal size, the so-called Johann shift.<sup>22</sup> An equivalent calibration is carried out for H-like Ar using the Ly $_{\alpha,1}$ , Ly $_{\alpha,2}$ , resonance lines and the T and J dielectronic satellite lines.

The location of the ellipses can also be used to calibrate position and orientation of the detector plane relative to the crystal. Shifts in the detector location of a few millimeters, out of 1.25 m, are easily observable when examining the residual between the predicted and measured ellipses. Currently, this is accomplished assuming a 0D crystal, outlined in detail in Ref. 17. This provides sufficient accuracy to determine the chord paths through the plasma for each pixel. The relative change in the Johann shift across the detector plane for HIREXSR is estimated to lead to changes of  $<0.1$  mm in the spectral direction, or sub-pixel shifts in the expected line-centers. Future work will include the finite crystal effects on the ellipse position in order to use the  $\lambda$ -calibration data to determine the detector position accurately enough to estimate the variation in focus across the detector. This technique can be validated by using precision translation and rotation stages to adjust the crystal/detector alignment in a known manner.

The instrumental broadening is estimated in two ways. The H-like Ar spectrum viewed by HIREXSR also includes a bright Mo<sup>32+</sup> line, and the different impurity masses leads to different Doppler widths for the same  $T_i$ . Assuming both impurities have the same temperature, the instrumental width,  $\Omega$ , can be determined. Uncorrected,  $T_{i,\text{Mo}} - T_{i,\text{Ar}} \sim 300$  eV, and by increasing the instrumental width, the corrected temperatures agree when  $\Omega \sim 0.27 \text{ m\AA}$ . This instrumental width corresponds to  $\sim 190$  eV offset in the ion temperature for H-like Ar. In high collisionality plasmas, comparing measured He-like Ar temperatures to  $T_e$  or  $T_i$  at large  $r/a$  from the edge CXRS system measuring B<sup>5+23</sup> also shows  $\sim 200$  eV difference. As mentioned in the end of Sec. III, if this instrumental width varies across detector, it can impact the reconstructed ion temperature profiles, although there is currently no evidence to support any significant non-uniformity. In practice, 200 eV is subtracted from all Ar-based  $T_i$  profiles output from the inversion routines.

## B. Binning

Since HIREXSR uses imaging detectors, the designation of spatial channels is not determined by the front end optics, in contrast to most CXRS systems which focus plasma light onto fiber optic cables. This allows soft x-ray spectra to be binned dynamically shot-to-shot or even frame-to-frame to suit different analysis needs. Spatial and temporal resolution can be relaxed to increase the number of photons per bin, increasing the accuracy of the toroidal rotation profile reconstruction. Alternatively bins limited only by the spatial resolution of the instrument could be used to find the scale length of the impurity density gradient which requires fewer photons. A single set of calibration data is assumed for each discharge, but THACO allows for multiple binning configurations and resulting inverted profiles to be stored in parallel MDSPlus trees nodes.

Figure 2 shows an example of how the raw image can be decomposed into spatial channels. Since the spectral and spatial calibration identifies a wavelength, intensity, and line of sight for each pixel, the user-defined bins simply collect a group of pixels and organizes them according to  $\lambda$ . This technique is robust to the emergence of damaged pixels since they can simply be thrown out at this stage as identified. For channels near the center of the detector (Figure 2(b)), the wavelength values are redundant but near the edges, the optics bend the spectral line over the pixel boundaries and the pixels defined by the bin result in a smooth line profile (Figure 2(c)). In order to reduce the duration of the nonlinear fitting stage, the spectra are averaged over a user-defined number of neighboring values of  $\lambda$ . This is done using a number of pixels less than or equal to the number of rows in the bin, ensuring spectral resolution is not downgraded. The line of sight that describes the channel is found by averaging the views of the collected group of pixels.

## C. Fitting and moment generation

In order to generate the spectral moments (3) for input to the inversion, contaminating lines and the background signal must first be removed from the region of interest. This is completed by using MPFIT<sup>24</sup> to find the nonlinear least-squares fit of a sum of Gaussians to the observed spectrum. While the line-integrated spectra are in general not Gaussian, but rather the sum of many shifted and broadened Gaussians, this fitting ansatz has been found to be acceptable in plasmas with low Mach shear. Figures 3(a) and 3(b) show the fit results to the He-like Ar spectrum consisting of the  $n = 2$  satellites (q,r,a,j,k) and the forbidden transition (z). In this spectrum, the capabilities of MPFIT are used constrain the fit using atomic physics. The relative shift and width of the q-r-a lines are defined to be the same and the j-line, nearly degenerate with the z-line, is fully constrained by the height, shift, and width of the k-line. This process is also used for the Lyman- $\alpha$  line pair and dielectronic satellites in the H-like Ar spectrum.

Broadband background is often present in the spectra and must be subtracted. When signal to background is high, moments are generated by numerically integrating the post-subtraction spectral brightness profile, Figure 3(c), using IDL's native 5-point Newton Cotes routine, INT\_TABULATED. Convergence tests varying the  $d\lambda$  of the integration interval symmetrically about the rest wavelength demonstrate asymptotic behavior in all three moments, although the uncertainty in  $M_1$  and  $M_2$  increases noticeably with  $d\lambda$ . As the background level increases, the uncertainty due to its subtraction begins to overwhelm the first and second moments computed using integration. When signal/background photons drop below 4, the moments are determined from the Gaussian fit with corresponding uncertainties in the shift and width determined by MPFIT.

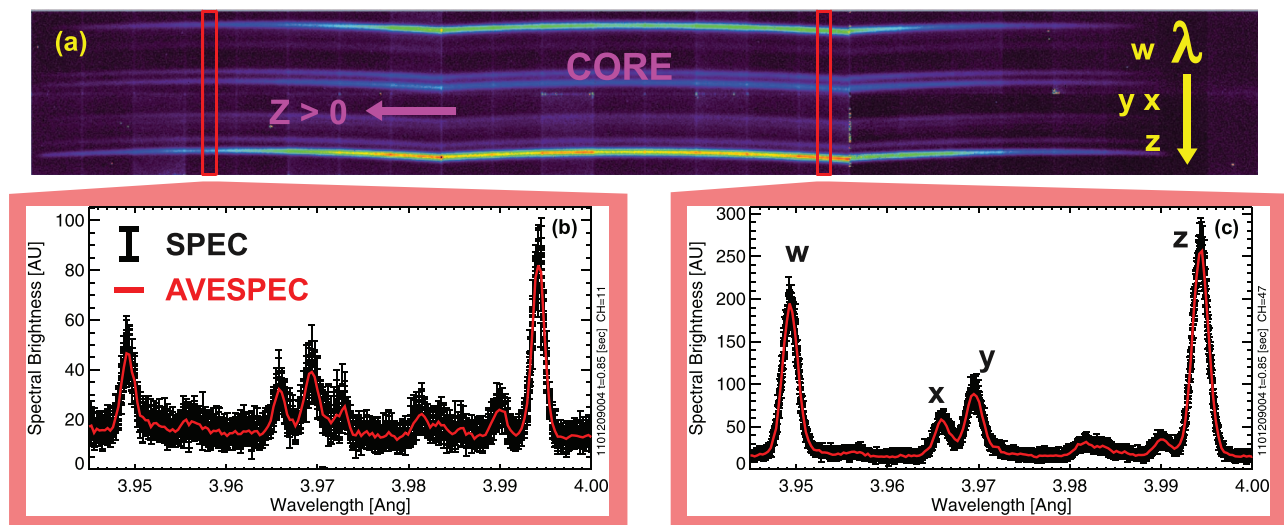


FIG. 2. Composite image from the  $\times 3$  PILATUS detectors showing the He-like spectra over the entire plasma cross section (a). Examples of spectra defined by the binning setup discussed in Sec. III are shown in (b) and (c) where the raw (SPEC) data are averaged (AVESPEC) prior to fitting and moment calculations.

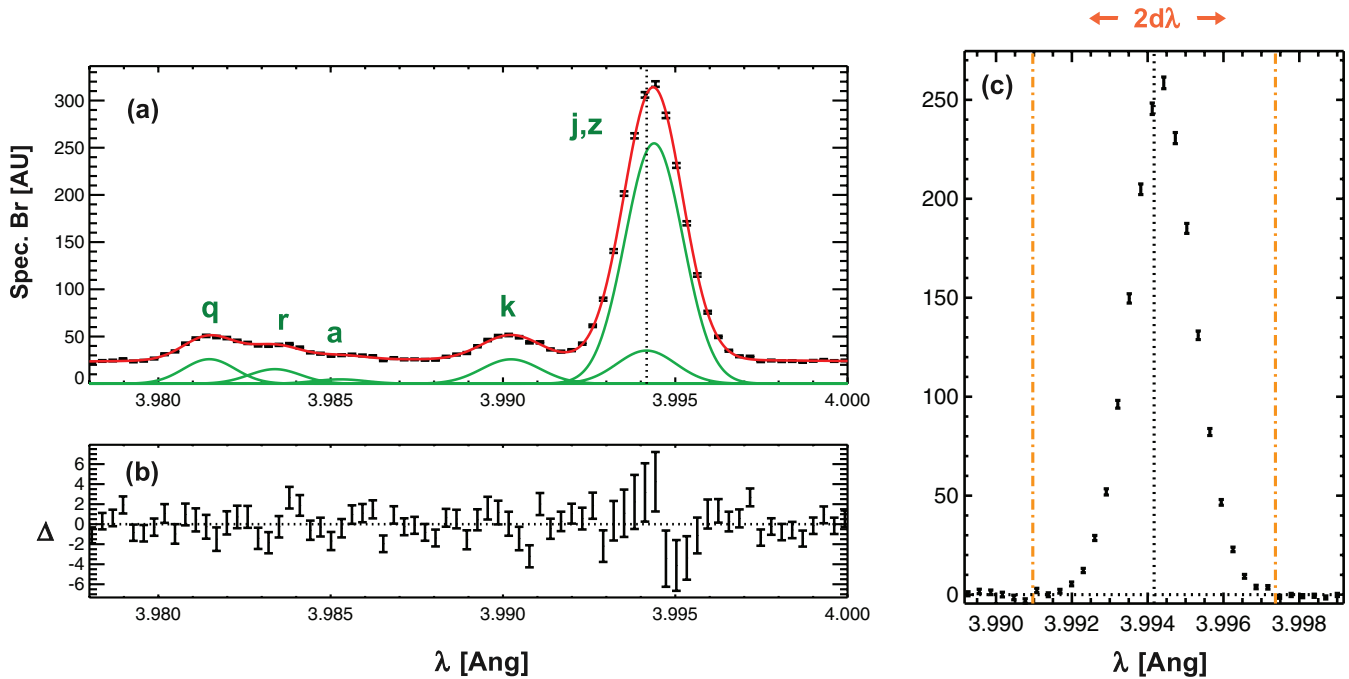


FIG. 3. A multi-peak Gaussian fit is made to the line-integrated He-like Ar spectrum (a) shown to have a small residual (b). Using this fit, the baseline and neighboring lines are removed to determine the pure z-line profile (c) from which the moments are found by numerically integrating (2).

#### D. Inversion

Example moment profiles for the z-line in an EDA H-mode plasma are plotted in Figure 4, where small CH#s are lines of sight below the midplane, while large CH#s view  $Z > 0$ . There is insufficient spatial coverage to invert these data without making assumptions on the symmetry of the plasma properties,  $\varepsilon$ ,  $v$ , and  $T_i$ . For the  $\text{Ar}^{16+}$  measurement, the entire poloidal cross section is resolved, so an  $m = 1$  sine term is resolvable in the inversions and the  $(R, Z)$  variation of the plasma is assumed to be of the form:

$$\begin{aligned} \varepsilon(R, Z) &= \varepsilon_o(\psi) + \varepsilon_s(\psi) \sin \theta, \\ \mathbf{v}(R, Z) &= [\omega_o(\psi) + \omega_s(\psi) \sin \theta] R \hat{\phi}, \\ T_i(R, Z) &= T_i(\psi) + T_{i,s}(\psi) \sin \theta. \end{aligned} \quad (6)$$

The  $m = 1$  terms are not included when analyzing H-like Ar moment profiles, as the required poloidal coverage is not available. The inclusion of the sine term in the emissivity is well motivated physically, since up/down asymmetries in impurity density have long been observed in tokamak plasmas.<sup>25</sup> The presence of a sine term in the toroidal rotation,  $\omega_s$ , is not expected based on the form of the 1st order neoclassical velocity,  $\mathbf{v} = u(\psi) \mathbf{B} + \omega(\psi) R \hat{\phi}$ .<sup>26</sup> Instead, the systematic presence of  $|\omega_s/\omega_o| > 0$  is an indicator of poloidal rotation which requires further scrutiny. Large up/down asymmetries in the ion temperature are also not expected, but have already been used to spatially calibrate the view as mentioned in Sec. II. Instead, the presence of a significant  $m = 1$  component in  $T_i$  is used as a metric of unexpected or unknown systematic error encountered in the tomographic analysis.

Details on the hyperbola tracing used to calculate the voxel matrix elements,  $V_{ji}$ , can be found in Appendix C of Ref. 25. This matrix is used to invert both the 0<sup>th</sup> and 2<sup>nd</sup> moment equations. Inversions are done in normalized poloidal flux,  $\psi_n$ , since in this coordinate system the on-axis derivative goes to zero and ion temperature profiles are observed to be more linear, better satisfying the regularization assumption. A non-uniform radial grid of  $\psi_n$  is used to account for the spectrometer's spatial resolution which while constant in physical space, allows for an increased resolution in  $\psi_n$  near the axis. To invert the 1<sup>st</sup> moment, a modified voxel matrix must be computed based on the assumed form of the velocity vector. For the solid body toroidal rotation specified in (6),  $\mathbf{v} = \omega R \hat{\phi}$  and the toroidal unit vector of the view is  $\hat{l}_j = \cos(\gamma_j) R_{T,j} / R$ , with  $\gamma_j$  being inclination angle of the view and  $R_{T,j}$  its tangency radius. This reduces the term inside the sum over  $i$  in the first moment equation in (3) to  $V_{ji} \cos(\gamma_j) R_{T,j} \omega_i \varepsilon_i$ . All the subscript  $j$  terms are collected into a new weighting matrix and the inversion solves for the radial profile of the emissivity-weighted toroidal rotation frequency  $(\omega \varepsilon)_i$ . Details on calculating the weighting matrix and inverting the 1<sup>st</sup> moment equation in the presence of toroidal and poloidal rotation are documented in Ref. 17.

All profiles are inverted using the least-squares technique described in Sec. III. In Figure 5, the emissivity (a), toroidal rotation (b), and temperature profiles (c) are plotted versus  $\psi_n$ , and correspond to the moment profiles shown in Figure 4. Included in Figure 4 are green curves computed by multiplying the derived profile by the appropriate weighting matrix, i.e., solving the forward rather than the inverse problem, and provide a useful check on the quality of the inversions. In Figure 4(c) the dash-dot green line is the profile that is

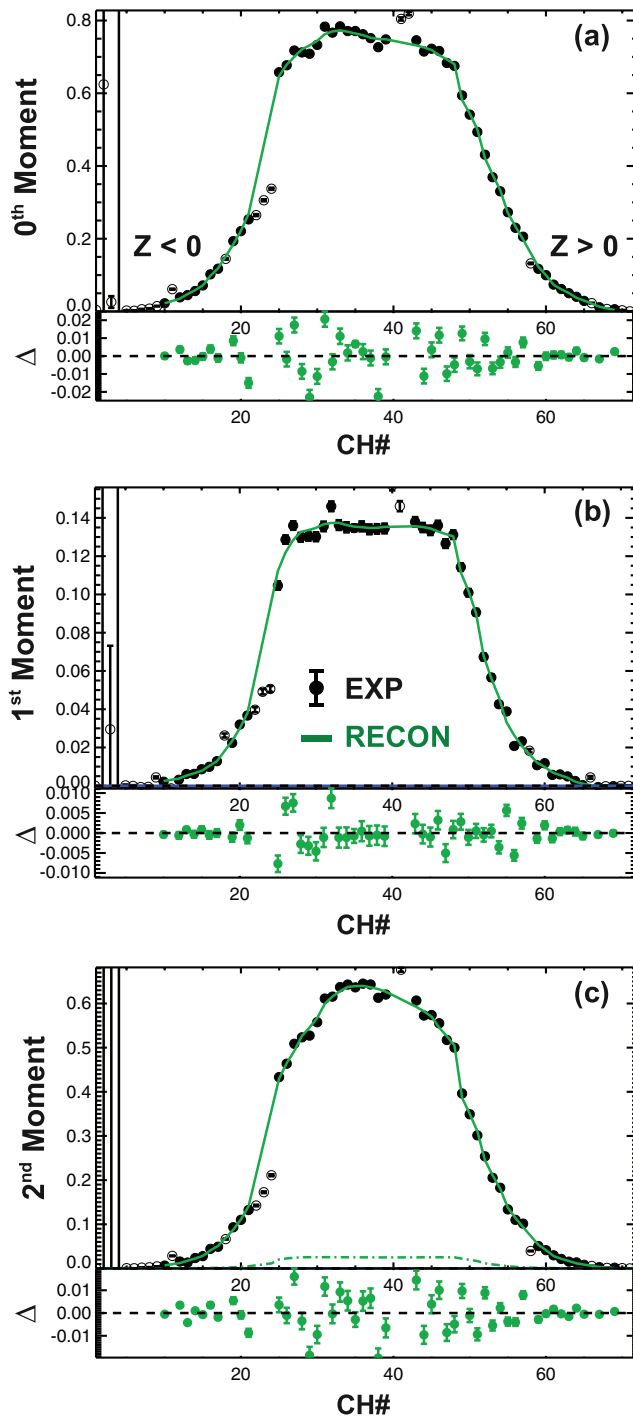


FIG. 4. Example 0th (a) 1st (b), and 2nd (c) moment profiles for the He-like z-line. Open circles are channels omitted from the reconstruction due to known detector problems or failed fits. The green line represents the profile calculated using the least-squares solution from the inversions, and is used as a check on the quality of the reconstruction.

subtracted from the second moment profile prior to the inversion representing the effect of taking the moment about the unshifted line center. In this particular H-mode, the rotation profile is relatively flat, and the local  $\omega$  (black) found from the inversion are similar to  $\omega$  computed from the line-integrated spectra (red). This is not case for the inverted and line-integrated ion temperature data shown in Figure 5(c). At  $\psi_n \sim 0.4$  the two begin to diverge, out-

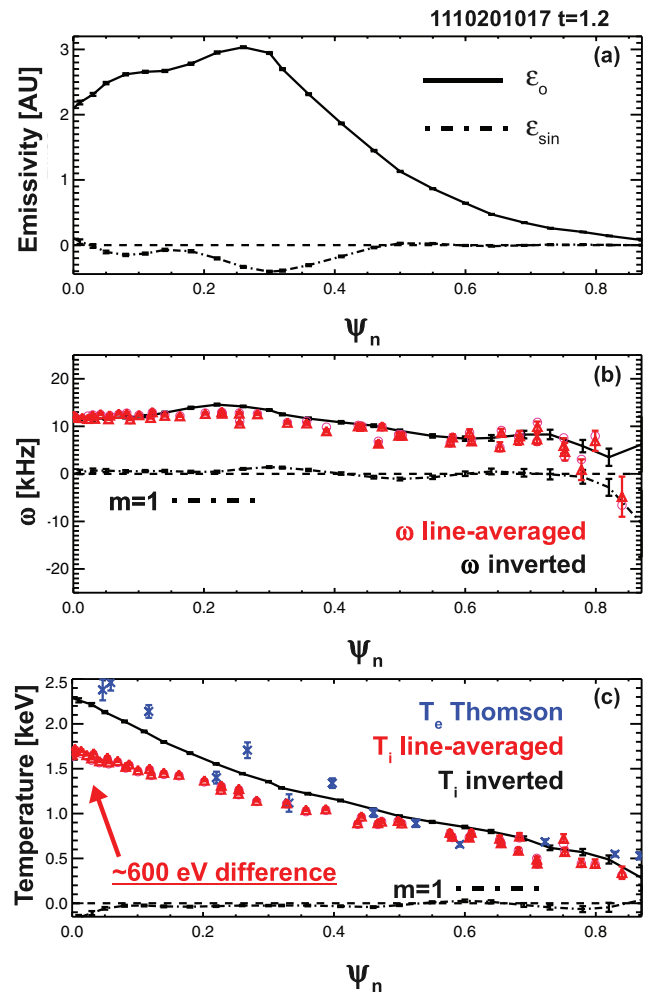


FIG. 5. Radial profiles of the emissivity (a), toroidal rotation frequency (b), and ion temperature (c) for an EDA H-mode plasma computed from the moment profiles shown in Figure 4. All profiles have an  $m = 0$  profile (solid) and an  $m = 1$  sine (dash-dot) profile. Line-averaged rotation and temperature are shown in red in (b) and (c) and the electron temperature from Thomson scattering is included in (c).

side the peak of the emissivity profile near  $\psi_n \sim 0.3$ , and at the core the difference reaches nearly 600 eV. The inverted ion temperature profile is in reasonable agreement with  $T_e$  from Thomson scattering, as expected in a high-density,  $\bar{n}_e \sim 3.2 \times 10^{20} \text{ m}^{-3}$ , C-Mod H-mode plasma. Note that the error bars are extremely small over the profiles in Figure 5. While this accurately represents the propagation of photon statistics as detailed in the Appendix, the reality is that in many C-Mod H-mode plasmas, photon signal levels are so high as to lead to a negligible contribution to the uncertainty.

## V. EXPERIMENTAL RESULTS

THACO has been used to analyze HIREXSR data for a large number of recent experiments on impurity,<sup>15,25</sup> momentum,<sup>10,27</sup> and thermal transport.<sup>11,28</sup> Two highlights from I-mode plasmas<sup>29</sup> are included to show the capabilities and challenges of the diagnostic.

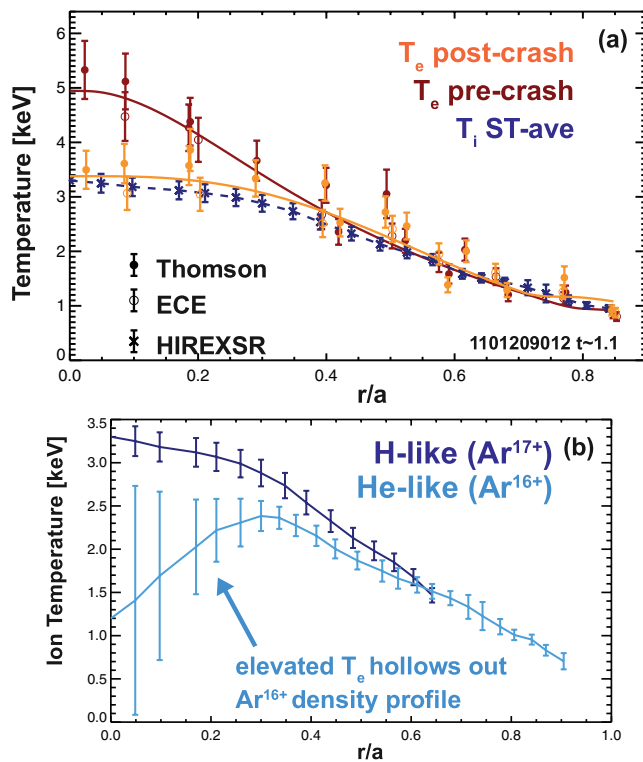


FIG. 6. Electron and ion temperature profiles in an I-mode plasma showing the sawtooth averaged  $T_i$  profile is consistent with the post-crash  $T_e$  profile (a). The ion temperature profile is reconstructed using both the He-like and H-like data (b).

### A. I-mode temperature profiles

The time-averaged ion temperature profile in an I-mode plasma determined using both the He-like and H-like data is shown in Figure 6(a). Included are electron temperature profiles from Thomson scattering and electron cyclotron emission,<sup>30</sup> one just prior to a sawtooth crash and another immediately following it. While the variation in  $T_e$  is above  $\sim 1.5$  keV and the fast time evolution can be resolved, the  $T_i$  variation can be estimated from the fractional change in the neutron rate, and estimated to be only a few hundred eV. With  $n_{e,0} \sim 2.5 \times 10^{20} \text{ m}^{-3}$ , the on-axis ion-electron power flux due to collisions is quite large,  $Q_{ie} \sim 4 \text{ MW/m}^3$ , in the later phase of the sawtooth, which should work to equilibrate  $T_i$  and  $T_e$ . But, this  $T_e$  also increases the  $\tau_{ie}^E$ , the ion-electron energy equilibration time constant, which becomes over a factor of two longer than the sawtooth period. This is thought to keep  $T_i$  down near the post-crash  $T_e$  profile, suggesting a large increase in core ion temperature may be possible with sawtooth stabilization. The physics of core thermal transport in I-mode plasmas can be investigated in more detail by using the 2 ms exposure operation of HIREXSR to develop composite profiles evolving over the sawtooth cycle using several 100 ms of repeatable sawteeth. This technique has already been successfully demonstrated for the He-like Ar z-line emissivity in L-mode plasmas.<sup>31</sup>

Due to the elevated  $T_e$ , the He-like argon density profile becomes hollow in I-mode plasmas, increasing the difficulty of reconstructing the core temperature and flow profiles with

a single charge state. In Figure 6(b), the ion temperature profiles from both  $\text{Ar}^{16+}$  and  $\text{Ar}^{17+}$  are over plotted revealing differences outside of stated error bars in the core. In this case the He-like Ar  $m = 1$   $T_i$  profile has been added in quadrature with its photon statistics uncertainty, both of which become large inside  $r/a \sim 0.3$ . Ideally,  $T_i$  profiles from both charge states should overlap within error bars, allowing an uncertainty weighted average to be a robust way of combining the data. While there is generally always an overlap region where  $T_{i,\text{He}}$  and  $T_{i,\text{H}}$  are equivalent, the details on how the data are combined impact the accuracy of  $\nabla T_i/T_i$  and are under investigation. More recent I-mode studies have modified HIREXSR to observe H-like Ar emission over the full plasma cross-section to enable better accuracy at elevated electron temperatures.

### B. I-mode radial electric field profiles

The HIREXSR spectrometer measures all the kinetic profile components necessary to reconstruct the radial electric field from radial force balance.<sup>32</sup> Figure 7 shows the various terms in an I-mode plasma, where the toroidal rotation (solid) is by far the strongest term, with the diamagnetic component (dash-dot) reduced by the  $1/Z$  dependence. The  $\nabla \ln(n_z)$  term is computed using the output of a steady-state impurity transport simulation<sup>31</sup> constrained by the observed emissivity profiles. Since the charge state density profiles are used to compute the density scale length for  $E_r$ , the diamagnetic terms in  $\text{Ar}^{16+}$  and  $\text{Ar}^{17+}$  can have different magnitudes and even signs. This is important when comparing rotation from the H-like and He-like argon in high-temperature, slowly rotating plasmas where diamagnetic flows could lead to expected differences between  $v_{\phi,\text{He}}$  and  $v_{\phi,\text{H}}$  of up to 10 km/s. While the full poloidal view of He-like argon emission allows the poloidal rotation to be found by comparing Doppler shifts for equivalent chords above and below the midplane,  $|v_{\theta}|$  can only be estimated within 1–2 km/s due to uncertainty in EFIT reconstructions used for mapping lines of sight. Except for so-called mode-conversion flow drive plasmas,<sup>33</sup> poloidal velocities in excess of 2 km/s have not been reliably observed on

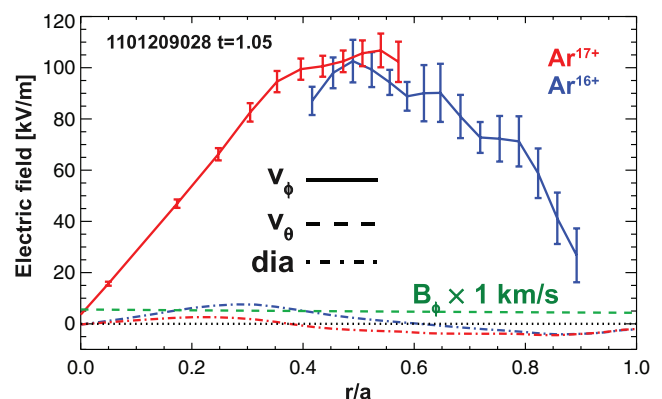


FIG. 7. Electron and ion temperature profiles in an I-mode plasma showing the sawtooth averaged  $T_i$  profile is consistent with the post-crash  $T_e$  profile (a). The ion temperature profile is reconstructed using both the He-like and H-like data (b).

Alcator C-Mod, using either HIREXSR or the previous array of von Hamos spectrometers. In practice, the error bar of the radial electric field is increased by  $v_\theta B_\phi$ , rather than its being added to the total  $E_r$ .

## VI. DISCUSSION

ITER and other large, high-density tokamak plasmas will not be able to use charge exchange spectroscopy as effectively as in present tokamaks, emphasizing the need to develop x-ray imaging crystal spectroscopy. In order to penetrate to the core, beams must be of order 1 MeV, much greater than the peak in the charge-exchange cross section for low-Z impurities.<sup>34</sup> A lower energy diagnostic neutral beam is planned for ITER, but core measurements will be limited by photon statistics, and the survivability of the plasma facing optics is a concern. In contrast, the plasma facing optic in ITER's planned crystal spectrometer<sup>35</sup> will be much farther removed from the plasma, reducing neutron flux and risk of plasma surface interactions, and by properly choosing the impurity species, the signal can be weighted to the core. While the locked-mode calibration methods described in Sec. IV have been successful on C-Mod, it is extremely unlikely that such techniques will be authorized on ITER, although a standard Ohmic plasma may be sufficient. The development of *in situ*, non-plasma based calibration schemes is desirable, and important for the future success of XICS.

The choice of tungsten, a non-recycling intrinsic impurity, is being considered as the species used for XICS on ITER.<sup>36,37</sup> The tungsten is expected to come from the diverter components, although reliable concentration estimates are not known. Based on experience with HIREXSR, when comparing the utility of extrinsic Ar and intrinsic Mo, argon is clearly the preferred choice. Substantial effort is put into minimizing the amount of Mo in C-Mod plasmas, and freshly boronized, high performance plasmas necessarily lack sufficient molybdenum signal for reliable inversions. Additionally, physics studies like intrinsic rotation in Ohmic plasmas<sup>10</sup> would be inaccessible if HIREXSR were designed only for molybdenum. Extrinsic seeding of trace high-Z noble gases (Ar, Kr, Xe) can be done relatively unobtrusively in present tokamaks, where the effect of increased core radiated power can generally be offset by increased input power.<sup>38</sup> For ITER, the prospect of increasing core radiation to enable diagnostics is unattractive given estimates of marginal H-mode accessibility. Arguably, the power into the pedestal required to maintain high edge temperature and global energy confinement,  $H_{98} \sim 1$ , is not known to within a few MW. Any exhaust power in excess of that needed to maintain the pedestal is better removed from the core plasma via radiation to the bulk PFCs, rather than added to the burden already being placed on the divertor PFCs via x-point radiation and conducted heat flux. The use of an extrinsically controllable impurity for use with XICS is attractive if the diagnostic is to be used in feedback control of core rotation and/or temperature profiles on ITER or other burning plasmas. In this case, the ability to observe the plasma's kinetic properties is not linked to erosion and sputtering of PFCs that could be driven by the heating, flow, and current drive ac-

tuators. In the future, THACO's forward modeling and inversion routines could be used to estimate the absolute impurity density needed to meet the accuracy requirements in the design specifications. The ability for THACO to handle non-uniform instrumental broadening opens the possibility to increase the crystal size without sacrificing accuracy, increasing throughput, requiring smaller fractions of extrinsic impurities.

Complications with the planned layout of the ITER core x-ray crystal spectrometer have been identified as well. Currently, only the top half of the plasma will be viewed, with a fan-like array, a design which can be demonstrated to be sensitive to poloidal variation in impurity density. Figure 8 shows reconstructions of temperature profiles (c) and (d) for viewing geometries (a) and (b) under various assumptions of  $n_z(\psi, \theta)$ ,

$$n_z(\psi, \theta) = n_{z,o}(\psi) + n_{z,\sin}(\psi) \sin \theta + n_{z,\cos}(\psi) \cos \theta. \quad (7)$$

Here,  $n_{z,\sin}$  represents an up/down asymmetry of impurity density and  $n_{z,\cos}$  an in/out asymmetry. Recent Alcator C-Mod studies of parallel transport of high-Z impurities have demonstrated changes in  $n_{z,\sin}/\langle n_z \rangle \sim 0.1$  that cannot be predicted by theory, and  $n_{z,\cos}/\langle n_z \rangle \sim 0.5$  can be expected for tungsten on ITER.<sup>25</sup>

Both poloidally asymmetric and symmetric  $n_z$  profiles, along with flux-surface symmetric  $T_e$  and  $n_e$  are used to form line-integrated spectra for LFS→HFS views covering the top half of the plasma. A slightly hollow emissivity profile is defined, peaking at  $r/a \sim 0.4$  with the ratio of peak to on-axis emissivity being  $\sim 1.7$ . Two limiting cases of viewing geometry are used, one with parallel views (Figure 8(a), green), resembling the C-Mod spectrometer, and other with substantial variation in the inclination angle of chords (Figure 8(b), red), closer to the layout planned for ITER. Experimental C-Mod profiles are used as to calculate the line-integrated spectra, and THACO is used to analyze and invert the synthetic spectra. When the impurity emission is poloidally symmetric (solid lines), both views reconstruct the assumed  $T_i$  profile (black) nearly exactly, as expected. When the plasma is up/down asymmetric (broken lines), Figure 8(c), systematic errors in the  $T_i$  profile are noticeable in both reconstructions for  $r/a < 0.3$ , just inside the peak of the emissivity profile. In contrast only the angled view incorrectly predicts the  $T_i$  profile under a substantial in/out asymmetry, Figure 8(d), as the parallel view effectively averages over the cosine term. Modifying the layout to have a full poloidal view with nearly parallel lines of sight, like HIREXSR, would make the instrument much less sensitive to  $n_z(\theta)$ . Since the impact of the asymmetry is felt strongest as the emissivity profile becomes hollow, another option would be to maintain a sufficiently wide spectral range to allow measurement of multiple charge states, ensuring a peaked emissivity is always seen as  $T_e$  is varied. Also, the poloidal variation of the high-Z emission could be characterized with a separate diagnostic allowing *a-priori* information about the asymmetry to be included in the inversion.

Another complication for XICS on ITER and high  $T_e$  operations on present tokamaks comes from the natural line broadening of high-Z impurities. The Ar K-shell lines have

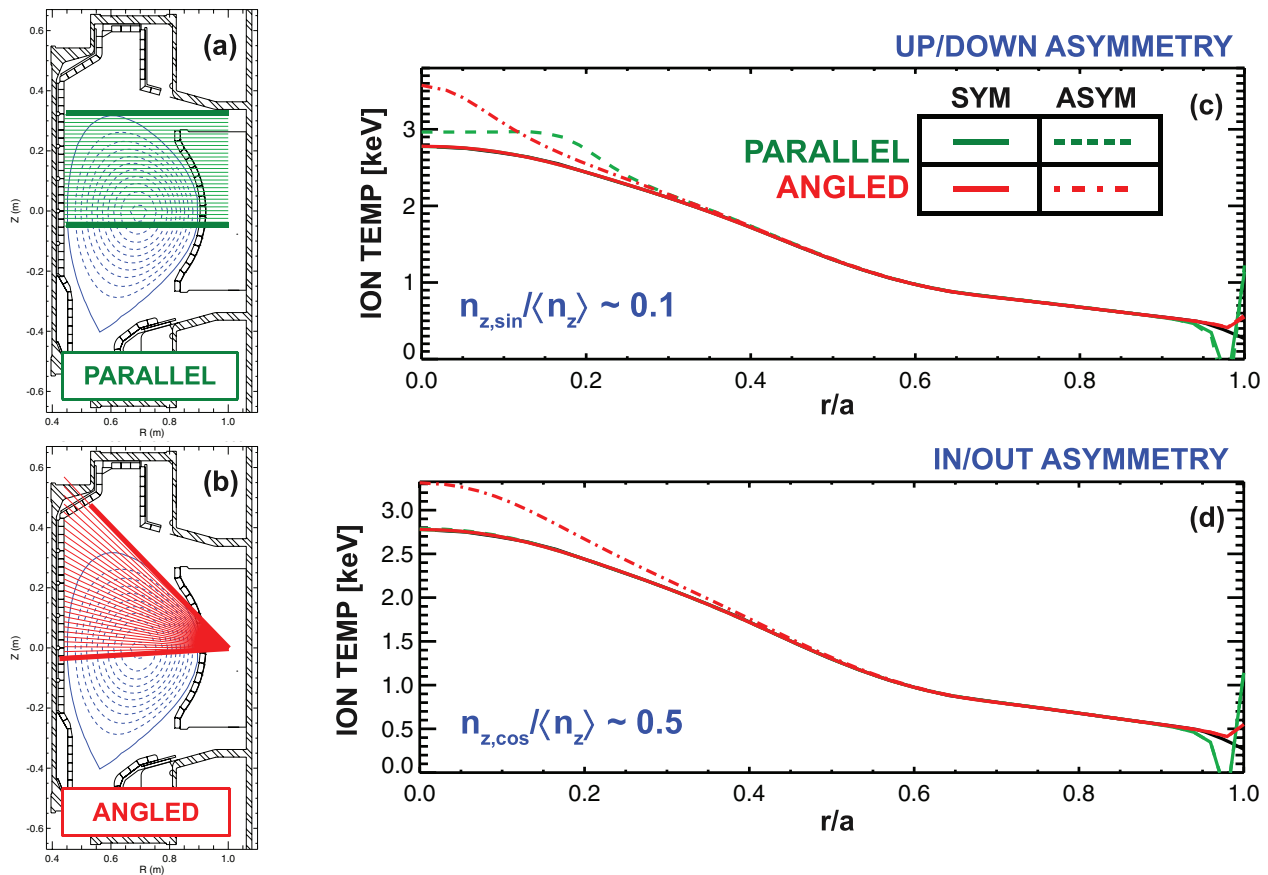


FIG. 8. Demonstration of systematic errors in the inverted  $T_i$  profiles for views with limited spatial coverage when the impurity density varies on a flux surface. Both parallel (a) and angled (b) views are sensitive to even small,  $n_{z,\sin}/\langle n_z \rangle \sim 0.1$ , up/down asymmetries (c) while the angled view is also sensitive to strong,  $n_{z,\cos}/\langle n_z \rangle \sim 0.5$ , in/out asymmetries (d).

transition rates,  $A_{ij}$ ,  $\sim 3 \times 10^{13} \text{ s}^{-1}$  and  $1 \times 10^{14} \text{ s}^{-1}$  for the  $\text{Ly}_{\alpha,1}$  ( $1s-2p$ ) and w-line ( $1s^2-1s2p$ ), respectively. As discussed in Sec. III, the result of the natural line broadening is to make the observed line shape a Voigt profile rather than a Gaussian. If this is ignored, the  $T_i$  found from a pure Gaussian fit is overestimated by  $< 50 \text{ eV}$  for  $\text{Ly}_{\alpha,1}$ , 1 and  $\sim 100 \text{ eV}$  for the w-line. While possibly impacting the accuracy of  $\nabla T_i/T_i$  profiles in argon-based XICS, the strong increase in natural line broadening,  $\sim Z^4$ , and the decrease in the Doppler width by  $\sqrt{m_z}$  means the effect becomes important as increased  $T_e$  forces the use of higher Z impurities. Analytically, the 2<sup>nd</sup> moment does not converge for a Voigt line shape, complicating the moment analysis. In practice, the moment integrals are taken over a limited  $d\lambda$  range where one can approximate the line-shape as the sum of Gaussians with the same line center. This ansatz carries through the moment equations in a similar manner as the instrumental function discussed in the Appendix, with  $\Delta = 0$ ,  $w_i^2 = 0$ , and the  $\Omega_{jk} \rightarrow \Omega_{ik}$  as the widths are a function of the known natural line width and the desired ion temperature. Rather than having  $T_i$  be proportional to  $w_i^2$ , there will be a nonlinear, non-analytic relationship between  $T_i$  and  $\sum_k \varepsilon_{ik} \Omega_{ik}^2$ . To avoid the natural line broadening, the so-called forbidden transition, or z-line ( $1s^2-1s2s$ ), in He-like noble gas elements could be used. This is a meta-stable state, leading to much smaller transitions rates, for  $\text{Ar}^{16+}$   $A_{ij} \sim 10^6 \text{ s}^{-1}$ , making natural line broadening completely negli-

gible. While the effect of natural line broadening is ignored in THACO due to the common use of  $\text{Ly}_{\alpha,1}$  and the z-line on C-Mod, future work will include these effects as HIREXSR is upgraded to view He-like Kr to allow core ion temperature measurements in I-mode plasmas where  $T_{e,o} > 9 \text{ keV}$  have been achieved.

## VII. CONCLUSION

X-ray imaging crystal spectrometers have begun to be deployed on magnetic fusion energy experiments, and similar instruments are expected to be critical tools used to diagnose the core plasma in ITER. XICS measures spectral emission from partially ionized impurities which is line-integrated through the plasma volume, requiring the use of Doppler tomography to determine the local emissivity, flow, and temperature data. This work details extensions made to the Doppler tomography technique as part of a larger package of software tools (THACO) used to analyze data from the Alcator C-Mod crystal spectrometer. While deployed locally, development of the THACO was completed with community-wide use in mind, generically approaching the tasks of calibration, binning, fitting, and moment generation as well as profile inversion. These advances have enabled new or expanded studies of impurity, momentum, and heat transport in Alcator C-Mod plasmas.

## ACKNOWLEDGMENTS

The authors would like to thank the engineering, technical and computing staff at the PSFC and PPPL for helping to make HIREXSR such a dramatic success. This work was supported by (U.S.) Department of Energy (DOE) contracts DE-FC02-99ER54512 and DE-AC02-09CH11466 and in part by an appointment to the DOE Fusion Energy Postdoctoral Research Program administered by ORISE.

## APPENDIX: EXTENSIONS TO DOPPLER TOMOGRAPHY

According to (5), the three inverse problems result in multiplying a matrix of known values into the experimental moment profiles:

$$\begin{aligned}\vec{\varepsilon} &= \mathbf{D} \cdot \vec{M}_0, \\ \vec{\varepsilon}_v &= \mathbf{E} \cdot \vec{M}_1, \\ \vec{\varepsilon}_T &= \mathbf{F} \cdot (\vec{M}_2 - \vec{M}_{sub}).\end{aligned}\quad (\text{A1})$$

Here,  $\mathbf{D}$ ,  $\mathbf{E}$ , and  $\mathbf{F}$  are simply the pseudo-inverse matrices for the three moment equations as shown in (5). In an effort to better understand the accuracy of Doppler tomography, propagation of photon statistical error through the inversion has been computed analytically. The emissivity is found directly but to compute the local velocity,  $v_i$ , and the temperature,  $T_{z,i}$ , the weighted emissivity profiles are divided by the total line emissivity,  $\varepsilon_i$ ,

$$\begin{aligned}\varepsilon_i &= \sum_j D_{ij} M_{0,j}, \\ v_i &= \frac{\varepsilon_{v,i}}{\varepsilon_i} = \frac{\sum_j E_{ij} M_{1,j}}{\sum_j D_{ij} M_{0,j}}, \\ T_i &= \frac{\varepsilon_{T,i}}{\varepsilon_i} = \frac{\sum_j F_{ij} (M_{2,j} - M_{sub,j})}{\sum_j D_{ij} M_{0,j}}.\end{aligned}\quad (\text{A2})$$

Although the error in the  $\varepsilon$  and  $\varepsilon_v$  profiles or  $\varepsilon$  and  $\varepsilon_T$  profiles can be easily computed, simply taking  $\sigma_T/T = (\sigma_\varepsilon^2/\varepsilon^2 + \sigma_{\varepsilon_T}^2/\varepsilon_T^2)^{1/2}$  would not be valid since there is substantial correlated error between  $\varepsilon$  and  $\varepsilon_T$  due each of the moment profiles including the total number of photons,  $N_j$ . The spectral moments,  $M_n$ , can be expressed in terms of the basic statistical properties of an arbitrary intensity distribution  $P^\lambda(\lambda)$ : the total number of photons in the binned spectra,  $N$ , its centroid,  $\mu$ , and its variance,  $S^2$ :

$$\begin{aligned}M_{0,j} &= a_j N_j, \\ M_{1,j} &= a_j N_j (\mu_j - \lambda_o), \\ M_{2,j} &= a_j N_j (S_j^2 + (\lambda_o - \mu_j)^2).\end{aligned}\quad (\text{A3})$$

Here,  $a_j$ , are the scaling constants that convert number of photons to brightness units. The variance can be expressed as a

nonlinear combination of the spectral moments using (A3),

$$S_j^2 = \frac{M_{2,j}}{M_{0,j}} - \frac{M_{1,j}^2}{M_{0,j}^2}.\quad (\text{A4})$$

From the central limit theorem, the uncertainty in  $N$ ,  $\mu$ , and  $S$  can be expressed in terms of  $N$  and  $S^2$ ,<sup>39</sup>

$$\begin{aligned}\sigma_N^2 &= N_j, \\ \sigma_\mu^2 &= \frac{S_j^2}{N_j}, \\ \sigma_S^2 &= \frac{S_j^2}{2(N_j - 1)},\end{aligned}\quad (\text{A5})$$

independent of the specifics of  $P^\lambda(\lambda)$ . In practice,  $\sigma_N$ ,  $\sigma_\mu$ , and  $\sigma_S$  can also include the effect of a non-zero background as outlined in Ref. 39. This is omitted here for clarity, although it is included in the HIREXSR analysis. Using standard sensitivity analysis, the uncertainty in the computed  $\varepsilon_i$ ,  $v_i$ , and  $T_{z,i}$  can be determined with respect the uncertainty in  $N$ ,  $\mu$ , and  $S$  via partial differentiation:

$$\begin{aligned}\sigma_{\varepsilon,i}^2 &= \sum_j \left( \frac{\partial \varepsilon_i}{\partial N_j} \right)^2 \sigma_{N,j}^2, \\ \sigma_{v,i}^2 &= \sum_j \left( \frac{\partial v_i}{\partial N_j} \right)^2 \sigma_{N,j}^2 + \left( \frac{\partial v_i}{\partial \mu_j} \right)^2 \sigma_{\mu,j}^2, \\ \sigma_{T,i}^2 &= \sum_j \left( \frac{\partial T_i}{\partial N_j} \right)^2 \sigma_{N,j}^2 + \left( \frac{\partial T_i}{\partial \mu_j} \right)^2 \sigma_{\mu,j}^2 + \left( \frac{\partial T_i}{\partial S_j} \right)^2 \sigma_{S,j}^2.\end{aligned}\quad (\text{A6})$$

Using (A2) and (A5) in (A6) the  $\sigma_\varepsilon$ ,  $\sigma_v$ , and  $\sigma_T$  can be found at each point,  $i$ , in the plasma:

$$\begin{aligned}\sigma_{\varepsilon,i}^2 &= \sum_j (D_{ij} a_j)^2 N_j, \\ \sigma_{v,i}^2 &= \sum_j \left( \frac{E_{ij} a_j M_{1,j}}{M_{0,j} \varepsilon_i} - \frac{\varepsilon_{v,i}}{\varepsilon_i^2} D_{ij} a_j \right)^2 N_j + \left( \frac{E_{ij} M_{0,j}}{\varepsilon_i} \right)^2 \frac{S_j^2}{N_j}, \\ \sigma_{T,i}^2 &= \sum_j \left( \frac{F_{ij} a_j M_{2,j}}{M_{0,j} \varepsilon_i} - \frac{\varepsilon_{T,i}}{\varepsilon_i^2} D_{ij} a_j \right)^2 N_j + \left( \frac{2F_{ij} M_{1,j}}{\varepsilon_i} \right)^2 \frac{S_j^2}{N_j} \\ &\quad + \left( \frac{2F_{ij} S_j M_{0,j}}{\varepsilon_i} \right)^2 \frac{S_j^2}{2(N_j - 1)}.\end{aligned}\quad (\text{A7})$$

The impact of the uncertainty in the subtraction vector,  $M_{sub}$ , has been omitted which is acceptable for low Mach number plasmas. Note that for large values of  $\epsilon$ , (A7) will under predict the error since the elements of the  $\mathbf{D}$ ,  $\mathbf{E}$ , and  $\mathbf{F}$  matrices in (A1) will be dominated by the regularization matrix. One could extend (A6) to include a partial derivative with respect to  $\epsilon$ , but there is not a straight-forward means to evaluate what  $\sigma_\epsilon$  would be acceptable.

The impact of instrumental broadening is critical to achieving  $\nabla T_i/T_i$  profiles from XICS that are accurate enough for turbulence simulations. When using planar detectors to measure emission dispersed by a spherically bent crystal, the

result is a variation in the focus, and thus the instrumental line-width, across the detector plane. The other major source of broadening in a crystal spectrometer, the so-called Rocking curve error due to crystal imperfections, could also be different for chords that impact the crystal at a different angle of incidence. In general the measured spectral power,  $P_m^\lambda$ , will be the line-integrated  $P_{in}^\lambda$  convolved with an instrument function,  $I_f$ :

$$P_m^\lambda = P_{in}^\lambda \times I_f. \quad (\text{A8})$$

When inverting the data, any channel-to-channel variation in the instrument function must be taken into account. Otherwise changes in line-broadening due to de-focusing, for example, will be propagated through the inversion as changes in the actual temperature profile. While the instrument function is convolved with the total line-integrated spectral power, the distributive property allows the convolution to be done with the spectral emissivity,  $\varepsilon_\lambda$ , first, and then summed at the detector:

$$P_m^\lambda = \frac{U}{4\pi} \int dl \varepsilon_\lambda \times I_f. \quad (\text{A9})$$

The assumption is made that the instrument function can be represented by a sum of Gaussians,

$$I_{f,j} = \sum_k \frac{\alpha_{jk}}{\Omega_{jk} \sqrt{2\pi}} \exp \left[ -\frac{(\lambda - \Delta_{jk})^2}{2\Omega_{jk}^2} \right] \quad (\text{A10})$$

with the coefficients properly normalized so that  $\sum_k \alpha_{jk} = 1$ , making the integral over  $I_f$  also equal to unity. The impact of such an instrument function on the moment equations can be easily derived. The 0<sup>th</sup> moment equation remains unchanged, as the instrument function merely moves photons around the spectrum. The 1<sup>st</sup> and 2<sup>nd</sup> moment equations, (A11) and (A12), now include  $\Delta_{jk}$  and  $\Omega_{jk}^2$  terms representing the impact of the instrument function:

$$M_{1,j} = \frac{\lambda_o}{c} \sum_i^p V_{ji} \left( \hat{l}_j \cdot \mathbf{v}_i + \sum_k \alpha_{jk} \Delta_{jk} \right) \varepsilon_{o,i}, \quad (\text{A11})$$

$$M_{2,j} = \sum_i^p V_{ji} \varepsilon_{o,i} \left( \frac{\lambda_o^2}{c^2} (\hat{l}_j \cdot \mathbf{v}_i)^2 + w_i^2 + \sum_k \alpha_{jk} \Omega_{jk}^2 \right). \quad (\text{A12})$$

If  $\Delta_{jk}$  and  $\Omega_{jk}^2$  are channel specific then their effect must be from the moment equations prior to the inversion in the same manner as the  $M_{sub}$  is used to remove the contribution to the 2<sup>nd</sup> moment due to a non-zero Mach number. If these instruments are constant across all spatial channels,  $j$ , then the instrumental effect can be removed from the derived velocity and temperature profiles after the inversion.

<sup>1</sup>B. C. Stratton, M. Bitter, K. W. Hill, D. L. Hillis, and J. T. Hogan, *Fusion Sci. Technol.* **53**, 431 (2008).

<sup>2</sup>A. Ince-Cushman, J. E. Rice, M. Bitter, M. L. Reinke, K. W. Hill, M. F. Gu, E. Eikenberry, Ch. Broennimann, S. Scott, Y. Podpaly, S. G. Less, and E. S. Marmor, *Rev. Sci. Instrum.* **79**, 10E302 (2008).

<sup>3</sup>Y. Shi, F. Wang, B. Wan, M. Bitter, S. G. Lee, J. Bak, K. W. Hill, J. Fu, Y. Li, W. Zhang, A. Ti, and B. Ling, *Plasma Phys. Control. Fusion* **52**, 085013 (2010).

<sup>4</sup>S. G. Lee, J. G. Bak, U. W. Nam, M. K. Moon, Y. Shi, M. Bitter, and K. Hill, *Rev. Sci. Instrum.* **81**, 10E506 (2010).

<sup>5</sup>N. Pablant, M. Bitter, L. Delgado-Aparicio, M. Goto, K. W. Hill, S. Lazerson, S. Morita, A. L. Roquemore, D. Gates, D. Monticello, H. Nielson, A. Reiman, M. Reinke, J. E. Rice, and H. Yamada, *Rev. Sci. Instrum.* **83**, 083506 (2012).

<sup>6</sup>R. Bell, *Rev. Sci. Instrum.* **68**, 1273 (1997).

<sup>7</sup>I. Condrea, E. Haddad, B. C. Gregory, and G. Abel, *Phys. Plasmas* **7**, 3641 (2000).

<sup>8</sup>N. T. Howard, M. Greenwald, D. R. Mikkelsen, A. E. White, M. L. Reinke, D. Ernst, Y. Podpaly, and J. Candy, *Phys. Plasmas* **19**, 056110 (2012).

<sup>9</sup>M. L. Reinke, I. H. Hutchinson, J. E. Rice, N. T. Howard, A. Bader, S. Wukitch, Y. Lin, D. C. Pace, A. Hubbard, J. W. Hughes, and Y. Podpaly, *Plasma Phys. Control. Fusion* **54**, 045004 (2012).

<sup>10</sup>J. E. Rice, M. J. Greenwald, Y. A. Podpaly, M. L. Reinke, P. H. Diamond, J. W. Hughes, N. T. Howard, Y. Ma, I. Cziegler, B. P. Duval, P. C. Ennever, D. Ernst, C. L. Fiore, C. Gao, J. H. Irby, E. S. Marmor, M. Porkolab, N. Tsujii, and S. M. Wolfe, *Phys. Plasmas* **19**, 056106 (2012).

<sup>11</sup>C. L. Fiore, D. R. Ernst, Y. A. Podpaly, D. Mikkelsen, N. T. Howard, J. Lee, M. L. Reinke, J. E. Rice, J. W. Hughes, Y. Ma, W. L. Rowand, and I. Bespamyatnov, *Phys. Plasmas* **19**, 056113 (2012).

<sup>12</sup>J. E. Rice, F. Bombarda, M. A. Graf, E. S. Marmor, and Y. Wang, *Rev. Sci. Instrum.* **66**, 752 (1995).

<sup>13</sup>A. Ince-Cushman, "Rotation studies in fusion plasmas via imaging x-ray crystal spectroscopy," Ph.D. dissertation (Massachusetts Institute of Technology, 2008).

<sup>14</sup>See <http://www.dectris.com> for PILATUS description.

<sup>15</sup>N. T. Howard, "Experimental and gyrokinetic studies of impurity transport in the core of Alcator C-Mod plasmas," Ph.D. dissertation (Massachusetts Institute of Technology, 2012).

<sup>16</sup>L. A. Shmaenok, S. V. Golovkin, V. N. Govorun, A. V. Ekimov, N. N. Salashchenko, V. V. Pickalov, V. P. Belik, F. C. Schuller, A. J. H. Donne, A. A. Oomens, K. A. Prokhorov, S. S. Andreev, A. A. Sorokin, B. G. Podlaskin, and L. V. Khasanov, *Rev. Sci. Instrum.* **72**, 1411 (2001).

<sup>17</sup>M. L. Reinke, Y. Podpaly, and C. Gao, Technical Report PSFC/RR-11-9, Plasma Science and Fusion Center, 2012.

<sup>18</sup>S. M. Wolfe, I. H. Hutchinson, R. S. Granetz, J. Rice, A. Hubbard, A. Lynn, P. Phillips, T. C. Hender, D. F. Howell, R. J. LaHaye, and J. T. Scoville, *Phys. Plasmas* **12**, 056110 (2005).

<sup>19</sup>A. Graf, private communication (2011).

<sup>20</sup>J. A. Snipes, D. J. Campbell, T. C. Hender, M. von Hellermann, and H. Weisen, *Nucl. Fusion* **30**, 205 (1990).

<sup>21</sup>H. Weisen, M. von Hellermann, A. Boileau, L. D. Horton, W. Mandl, and H. P. Summers, *Nucl. Fusion* **29**, 2187 (1989).

<sup>22</sup>E. Wang, P. Beiersdorfer, M. Gu, M. Bitter, L. Delgado-Aparicio, K. W. Hill, M. Reinke, J. E. Rice, and Y. Podpaly, *Rev. Sci. Instrum.* **81**, 10E329 (2010).

<sup>23</sup>R. M. McDermott, "Edge radial electric field studies via charge exchange recombination spectroscopy on the Alcator C-Mod Tokamak," Ph.D. dissertation (Massachusetts Institute of Technology, 2009).

<sup>24</sup>C. B. Markwardt, e-print [arXiv:0902.2850](https://arxiv.org/abs/0902.2850) [astro-ph.IM].

<sup>25</sup>M. L. Reinke, "Experimental tests of parallel impurity transport theory in tokamak plasmas," Ph.D. dissertation (Massachusetts Institute of Technology, 2011).

<sup>26</sup>P. Helander and D. J. Sigmar, *Collisional Transport in Magnetized Plasmas* (Cambridge University Press, 2002).

<sup>27</sup>Y. A. Podpaly, "Rotation generation and transport in tokamak plasmas," Ph.D. dissertation (Massachusetts Institute of Technology, 2012).

<sup>28</sup>M. Porkolab, "Transport and turbulence studies in the linear Ohmic confinement regime in Alcator C-Mod," submitted to *Plasma Phys. Control. Fusion* (2012).

<sup>29</sup>D. G. Whyte, A. E. Hubbard, J. W. Hughes, B. Lipschultz, J. E. Rice, E. S. Marmor, M. Greenwald, I. Cziegler, A. Dominguez, T. Golfinopoulos, N. Howard, L. Lin, R. M. McDermott, M. Porkolab, M. L. Reinke, J. Terry, N. Tsujii, S. Wolfe, S. Wukitch, Y. Lin, and the Alcator C-Mod Team, *Nucl. Fusion* **50**, 105005 (2010).

<sup>30</sup>N. P. Basse, A. Dominguez, E. M. Edlund, C. L. Fiore, R. S. Granetz, A. E. Hubbard, J. W. Hughes, I. H. Hutchinson, J. H. Irby, B. LaBombard, L. Lin, Y. Lin, B. Lipschultz, J. E. Liptac, E. S. Marmor, D. A. Mossessian,

- R. R. Parker, M. Porkolab, J. E. Rice, J. A. Snipes, V. Tang, J. L. Terry, S. M. Wolfe, S. J. Wukitch, K. Zhurovish, R. V. Bravenec, P. E. Phillips, W. L. Rowan, G. J. Kramer, G. Schilling, S. D. Scott, and S. J. Zweben, *Fusion Sci. Technol.* **51**, 476 (2007).
- <sup>31</sup>M. L. Reinke, A. Ince-Cushman, Y. Podpaly, J. E. Rice, M. Bitter, K. W. Hill, K. B. Fournier, and M. F. Gu, *AIP Conf. Proc.* **1161**, 52 (2009).
- <sup>32</sup>K. Ida, *Plasma Phys. Control. Fusion* **40**, 1429 (1998).
- <sup>33</sup>Y. Lin, J. E. Rice, S. J. Wukitch, M. J. Greenwald, A. E. Hubbard, A. Ince-Cushman, L. Lin, E. S. Marmor, M. Porkolab, M. L. Reinke, N. Tsujii, J. C. Write, and Alcator C-Mod Team, *Phys. Plasmas* **16**, 056102 (2009).
- <sup>34</sup>D. Thomas, *Phys. Plasmas* **19**, 056118 (2012).
- <sup>35</sup>P. Beiresdorfer, J. Clementson, J. Dunn, M. F. Gu, K. Morris, Y. Podpaly, E. Wang, M. Bitter, R. Feder, K. W. Hill, D. Johnson, and R. Barnsley, *J. Phys. B* **43**, 144008 (2011).
- <sup>36</sup>P. Beiresdorfer, J. Dunn, and K. Morris, "ITER core imaging x-ray spectrometer conceptual design and performance assessment," Final report on subcontract ICP008450-R, June, 2009, see <http://www.pppl.gov/usiter-diagnostics>.
- <sup>37</sup>P. Beiresdorfer, J. Wen, J. Dunn, and K. Morris, Technical Report LLNL-SR-464953, Lawrence Livermore National Laboratory, 2011.
- <sup>38</sup>A. Loarte, J. W. Hughes, M. L. Reinke, J. L. Terry, B. LaBombard, D. Brunner, M. Greenwald, B. Lipschultz, Y. Ma, S. Wukitch, and S. Wolfe, *Phys. Plasmas* **18**, 056105 (2011).
- <sup>39</sup>I. H. Hutchinson, *Eur. Phys. Jour. Plus* **127**, 81 (2012).